

# Oxygen-Substituted Porous C<sub>2</sub>N Frameworks as Efficient Electrocatalysts for Carbon Dioxide Electroreduction

Shuai Wang<sup>+</sup>, Shujie Zhou<sup>+</sup>, Zhipeng Ma<sup>+</sup>, Nana Gao, Rahman Daiyan, Joshua Leverett, Yihao Shan, Xiaofeng Zhu, Yufei Zhao, Qiang Liu, Rose Amal, Xunyu Lu, Tianxi Liu, Markus Antonietti, Yinguang Chen, Qingran Zhang,\* and Zhihong Tian\*

**Abstract:** The electrochemical carbon dioxide reduction reaction (CO<sub>2</sub>RR) provides a green avenue for decarbonizing the conventional chemical industries. Here, a structure–selectivity relationship of catalysts is pivotal for the control of a highly selective and active CO<sub>2</sub>RR pathway. We report the fabrication of an oxygen-substituted C<sub>2</sub>N as metal-free catalyst (O–C<sub>2</sub>N) for electrochemical CO<sub>2</sub>–to–CO conversion with tunable O microenvironment. Combined spectroscopic analysis reveals a fine tailored N–C–O moiety in O–C<sub>2</sub>N, where C–O–C species (e.g., ring in-plane ether) become the dominant oxygen configurations at higher pyrolysis temperatures. Based on experimental observations, a correlation between the exocyclic O-substituted N–C–O–C moieties and CO selectivity is established, giving clear chemical tools for active structure design. The optimized O–C<sub>2</sub>N electrocatalysts with the dominant appearance of C–O–C moieties exhibit an outstanding 2e<sup>−</sup> CO<sub>2</sub>RR performance with a CO selectivity up to 94.8%, which can be well maintained in a practical flow-cell reactor with an adjustable syngas feature.

## Introduction

Electrochemical carbon dioxide reduction reaction (CO<sub>2</sub>RR) provides a promising strategy to convert the excess of CO<sub>2</sub> into value-added chemicals and fuels, such as CO, which can be readily used as feedstock in further industrial synthesis (e.g., for Fischer–Tropsch process and tandem electrolysis), lowering the impact of chemical industry on CO<sub>2</sub>-related global warming.<sup>[1–3]</sup> Only when powered with renewable electricity, CO<sub>2</sub>RR offers an appealing solution to close the current carbon loop, accelerating the attainment of a carbon neutral economy with the simultaneous storage of intermittent renewable energy.<sup>[4,5]</sup> Nevertheless, despite significant progress, it still remains a grand challenge to develop highly active/selective CO<sub>2</sub>RR electrocatalysts with distinctive active structures for not only improving the CO<sub>2</sub>

reduction performance toward industrial demands (in terms of material cost, productivity, selectivity and stability) but also providing clear chemical tools for solid mechanism studies.<sup>[5,6]</sup>

The past decades have witnessed an advancement in developing various CO<sub>2</sub>RR electrocatalysts, ranging from noble metals, transition-metal-based oxides, chalcogenides, alloys to carbon-supported nanoparticles, single atoms, and atomic clusters.<sup>[7–11]</sup> Compared to metal-based counterparts, metal-free electrocatalysts hold great promises in expediting efficient CO<sub>2</sub>RR catalysis with cost-effectiveness, which is attributed to their abundant natural sources, tunable electronic properties, high electrical conductivity, good tolerance to toxic impurities and environmental benignity.<sup>[6,12]</sup> However, the pristine carbon itself is catalytically inert towards not only CO<sub>2</sub>RR but also other electrochemical reactions (e.g., water splitting and nitrogen fixation) due to

[\*] S. Wang<sup>+</sup>, Y. Chen, Q. Zhang  
 State Key Laboratory of Pollution Control and Resources Reuse,  
 School of Environmental Science and Engineering, Tongji University,  
 1239 Siping Road, Shanghai 200092, P.R. China  
 E-mail: qingran\_zhang@tongji.edu.cn  
 S. Zhou<sup>+</sup>, Z. Ma<sup>+</sup>, R. Daiyan, J. Leverett, Y. Shan, R. Amal, X. Lu  
 Particles and Catalysis Research Group, School of Chemical  
 Engineering, University of New South Wales, Sydney 2052, Australia  
 N. Gao, Z. Tian  
 Engineering Research Center for Nanomaterials, Henan University,  
 Kaifeng 475004, P.R. China  
 E-mail: zhihong.tian@henu.edu.cn  
 X. Zhu  
 State Key Laboratory of Environment-Friendly Energy Materials,  
 School of Materials and Chemistry, Southwest University of Science  
 and Technology, Mianyang 621010, P.R. China

Y. Zhao  
 Centre for Clean Energy Technology, University of Technology  
 Sydney, Broadway, Sydney NSW-2007, Australia

Q. Liu  
 School of Environmental and Chemical Engineering, Shanghai  
 University, Shanghai 200444, P.R. China

T. Liu  
 The Key Laboratory of Synthetic and Biological Colloids, Ministry of  
 Education, School of Chemical and Material Engineering, Jiangnan  
 University, Wuxi 214122, P.R. China

M. Antonietti  
 Department of Colloid Chemistry, Max Planck Institute of Colloids  
 and Interfaces, Potsdam 14476, Germany

[<sup>+</sup>] These authors contributed equally to this work.

Additional supporting information can be found online in the  
 Supporting Information section

the lack of reactive species.<sup>[13]</sup> This thusly necessitates the fine tailoring of their electronic properties for an improved CO<sub>2</sub> affinity and reactivity, such as through either heteroatom doping or defect engineering, which effectively disturbs the electronic symmetry of sp<sup>2</sup>-hybridized carbon skeleton thereby tuning their catalytic behaviour towards the CO<sub>2</sub>RR process.<sup>[14]</sup> During the past decades, N as an heteroatom element neighbouring to carbon in the periodic table has been studied extensively to afford efficient metal-free electrocatalysts. The higher electronegativity of N leads to a charge redistribution in the carbon skeleton (with N partially negatively charged, while neighbouring C is slightly positive), which in turn activates the  $\pi$  electron pool that facilitates the adsorption of Lewis acidic CO<sub>2</sub> molecules and those CO<sub>2</sub><sup>-</sup> intermediates, giving a reduced rate-determining overpotential and improved CO<sub>2</sub>RR activity.<sup>[15,16]</sup> For instance, early pioneering works have demonstrated the N-doped carbon nanotubes and graphene as efficient CO<sub>2</sub>RR catalysts for CO/formate formation, where their activity/selectivity depend largely on the N dopants/density.<sup>[17–19]</sup> Moreover, in other recent studies, it was suggested that the incorporation of N dopants may also generate structural defects and pores that are beneficial for CO<sub>2</sub>RR catalysis through a polarization effect, opening a promising avenue to afford high-performance metal-free electrocatalysts.<sup>[20]</sup> In these regards, further research interest has been encouraged to developing efficient N-doped carbon materials for an enhanced CO<sub>2</sub>RR activity, aiming to tailor their catalytic behaviours upon a precise active structure engineering.

Nonetheless, despite some progress, achieving an accurate control of active motifs within a N-incorporated defective carbon structure is still challenging due to the lack of programmable material engineering strategies, especially considering the irregular appearance of oxygen-terminated defects. To be specific, on the one hand, the formation of topological defects (e.g., pentagons and Thrower–Stone–Wales defects) or carbon vacancies in N-doped carbon catalysts during the high-temperature material synthesis procedure (such as chemical vapour deposition and thermal condensation) might be beneficial for an enhanced CO<sub>2</sub>RR activity due to the charge redistribution or polarization effect, as reported previously.<sup>[15,20]</sup> However, the as-formed defect sites may also react or interact strongly with the ubiquitous oxygen, forming undesirable oxygen functionalities that not only cover the catalytic N or defect sites but also complicate the investigation of genuine active species. All that hinders the rational improvement of CO<sub>2</sub>RR activity. Interestingly, on the other hand, oxygen functional groups (like aromatic ethers and epoxy) have also been identified as highly selective and comparably active species in various catalytic reactions, ranging from hydrogen peroxide electrosynthesis to dehydrogenation of n-butane.<sup>[21–23]</sup> Thus, it is plausible to postulate that those oxygen functionalities may even significantly contribute to CO<sub>2</sub>RR actively. For example, despite a poor electrochemical stability, carboxyl groups (–COOH) were evidenced as the apparent active species for the selective formate formation during CO<sub>2</sub>RR on a O-modified single layer graphene disk catalyst, but synergies between carboxyl and other types of oxygen functionalities (e.g., hydroxyl, epoxide and carbonyl)

are essential for an enhanced CO<sub>2</sub>RR performance.<sup>[24]</sup> This indicates the possible promoting role of oxygen-containing groups in CO<sub>2</sub>RR catalysis that deserve more intense analysis during the catalytic mechanism study. Moreover, previous theoretical as well as experimental studies all suggested an improved CO<sub>2</sub> adsorption behaviour on the O-functionalized carbon materials due to their strong electrostatic/van der Waals interactions with CO<sub>2</sub> molecules. All that promises to enhance the CO<sub>2</sub> electroreduction activity upon rational O modification process.<sup>[25,26]</sup> To this end, fine engineering the oxygen functionalities in N-doped defective carbon catalysts is highly sought after for not only obtaining a high CO<sub>2</sub>RR performance but also gaining deeper insights into the role of oxygen microenvironment in CO<sub>2</sub>RR catalysis. Compared to other oxygen functionalities, ether groups (and especially aromatic ethers) are thermally and electrochemically stable (unlike carbonyl O), and their catalytically active nature has already been well identified in other electrocatalytic reactions.<sup>[16,22,27]</sup> However, direct experimental evidence regarding the effect of ether O on the CO<sub>2</sub>RR performance is still missing, especially for a N-doped carbon catalysts.

Here, by adopting covalent carbon nitride (CN) as programmable two-dimensional (2D) template and monomer fragment source, we designed a well-defined, 2D-oxygen-substituted C<sub>2</sub>N (O–C<sub>2</sub>N) framework as efficient CO<sub>2</sub>RR electrocatalyst. This follows essentially the principles reported in our previous paper on C,N-doped layered C<sub>2</sub>Ns.<sup>[28,29]</sup> Using a heterocyclic reaction from gallic acid and dinitrile based fragments from the carbon nitride template, aromatic 1,4-oxazole rings are formed in high abundance, accessible by in-plane structural pores coming from the two-valent oxygen braking the carbon planes. As such, the oxazine- or dibenzodioxine-bridged C<sub>2</sub>N skeleton enables the appearance of abundant oxygen functionalities within the carbon catalysts, while the types of these O functional groups can be controlled deliberately. X-ray absorption spectroscopy (XAS) characterizations show a thermal transformation between different O functionalities in the O–C<sub>2</sub>N catalysts, where distinctive ether or epoxy O features as the dominant functional species at high temperatures, providing a clear chemical tool for investigating the origin of CO<sub>2</sub>RR selectivity upon a precise O modification. Interestingly, experimental observations reveal a positive correlation between the C–O–C moieties and CO selectivity. Benefited from the abundant oxygen dopants and a porous nature, the optimized O–C<sub>2</sub>N catalyst exhibits an outstanding 2e<sup>-</sup> CO<sub>2</sub>RR performance with a CO selectivity up to 94.8%, which can be also translated in a practical flow-cell reactor to create an adjustable syngas. To note, this work aims to not only develop high-performance CO<sub>2</sub>RR electrocatalysts with cost-effectiveness but also provide effective strategies to fabricate N,O-co-doped metal free carbocatalyst for in-depth chemical studies.

## Results and Discussion

To fabricate the O–C<sub>2</sub>N catalysts, we followed a previously published two-step pyrolysis procedure of a mixture containing both dicyandiamide (DCDA) and gallic acid under Ar

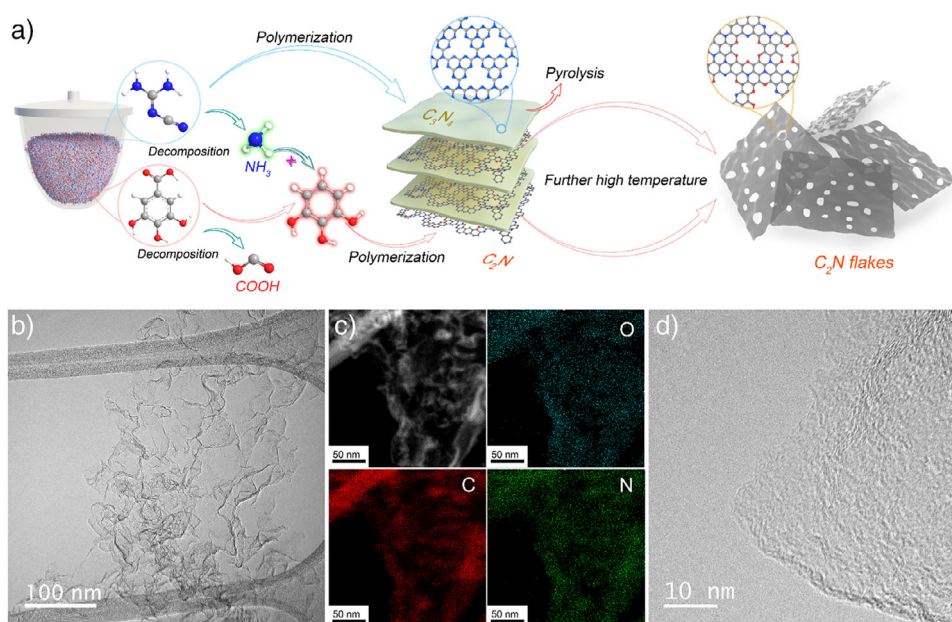


**Figure 1.** a) Schematic illustration of pyrolysis synthesis procedure of the sheet-like O–C<sub>2</sub>N 10 catalysts. b) TEM image of O–C<sub>2</sub>N 10. c) Scanning transmission electron microscopy (STEM) image and the corresponding EDS maps of O–C<sub>2</sub>N 10 for O, C and N. d) HR-TEM image of the O–C<sub>2</sub>N 10 catalyst.

atmosphere, as shown in Figure 1a.<sup>[28,29]</sup> During the pyrolysis, the DCDA firstly transfers into a layered graphitic carbon nitride (g–C<sub>3</sub>N<sub>4</sub>) as a hard template, which generates ample amount of NH<sub>3</sub> for a reductive environment. Meanwhile, following a decarboxylation process, the gallic acid decomposes gradually to yield pyrogallol rings for the subsequent N/O substitution (where simple heterocyclic reactions could take place easily). As a result, the pyrogallol-containing small molecules condensate with NH<sub>3</sub> at elevated temperatures, forming the O/N-rich C<sub>2</sub>N polymers that are templated by the simultaneously formed layered g–C<sub>3</sub>N<sub>4</sub> as programmable precursor mixture. Due to the different formation energy of those bonded N–C species and O functionalities, the N/O-substituted C configurations in the final carbon products could be readily fine-tailored by adjusting the condensation temperatures, where samples obtained at 800 °C, 900 °C, 1000 °C are labelled as O–C<sub>2</sub>N 8, O–C<sub>2</sub>N 9 and O–C<sub>2</sub>N 10, respectively.

To characterize the morphology of O–C<sub>2</sub>N 10, scanning electron microscopy (SEM) was first employed. It reveals that the O–C<sub>2</sub>N 10 consists of an interconnected macroscopic network of nanosheets, showing a scrambled feature on the micrometre scale (Figure S1). Transmission electron microscopy (TEM, Figures 1b and S2) measurements further confirm a scrambled nanosheet structure on O–C<sub>2</sub>N 10, which forms numerous open pores that should be beneficial for a rapid CO<sub>2</sub>RR mass transfer. Through the energy-dispersive X-ray spectroscopy (EDS) elemental mapping of a selected area on the O–C<sub>2</sub>N 10, it was validated that O, C and N elements are distributed uniformly across the nanosheet structure (Figure 1c), demonstrating the successful incorporation of O and N atoms into the carbon skeleton. As

expected, due to the effective heterocyclic reactions during the condensation of oxazines or dibenzodioxines derived from gallic acid, a high oxygen content was obtained for O–C<sub>2</sub>N 10 catalysts, as indicated by the large atom ratio of O/C (Table S1). Further performing the high-resolution TEM characterization (Figure 1d) indicated a randomly oriented structure on O-incorporated C<sub>2</sub>N frameworks, suggesting a possible turbostratic stacking (regular but not necessarily long-range ordered) of C<sub>2</sub>N planes with less obvious crystalline features. This can be further evidenced by the X-ray diffraction (XRD) measurements (Figure S3), showing no narrow Bragg diffraction peaks on the as-obtained O–C<sub>2</sub>N samples, which indicates the lack of obvious crystalline phases in those hybrid carbon catalysts, as reported previously.<sup>[30,31]</sup> Notably, by conducting the Brunauer–Emmett–Teller (BET) measurements (Figure 2a), it was indicated that all O–C<sub>2</sub>N catalysts possess a high specific surface area, giving 522, 486 and 548 m<sup>2</sup> g<sup>−1</sup> for O–C<sub>2</sub>N 8, O–C<sub>2</sub>N 9 and O–C<sub>2</sub>N 10, respectively. Moreover, calculated pore size distribution derived from the adsorption branch suggests a surface adsorption at the C<sub>2</sub>N layers, which are dominated with mesopores of the stacked nanosheets (Figure S4). Based on previous theoretical as well as experimental studies, the highly organized, straight transport pores and the high specific surface area of O–C<sub>2</sub>N are important to expedite a CO<sub>2</sub>RR process effectively, and the structure not only exposes more catalytically active species but also accelerates the mass transfer for a rapid adsorption/desorption of reactants/products.<sup>[30,32]</sup> Thus, the collective spectroscopic observations above all indicate the successful attainment of a O/N-rich porous nanosheet structure of O-modified C<sub>2</sub>N frameworks.

The chemical composition of O–C<sub>2</sub>N 10 was then investigated by X-ray photoelectron spectroscopy (XPS). For



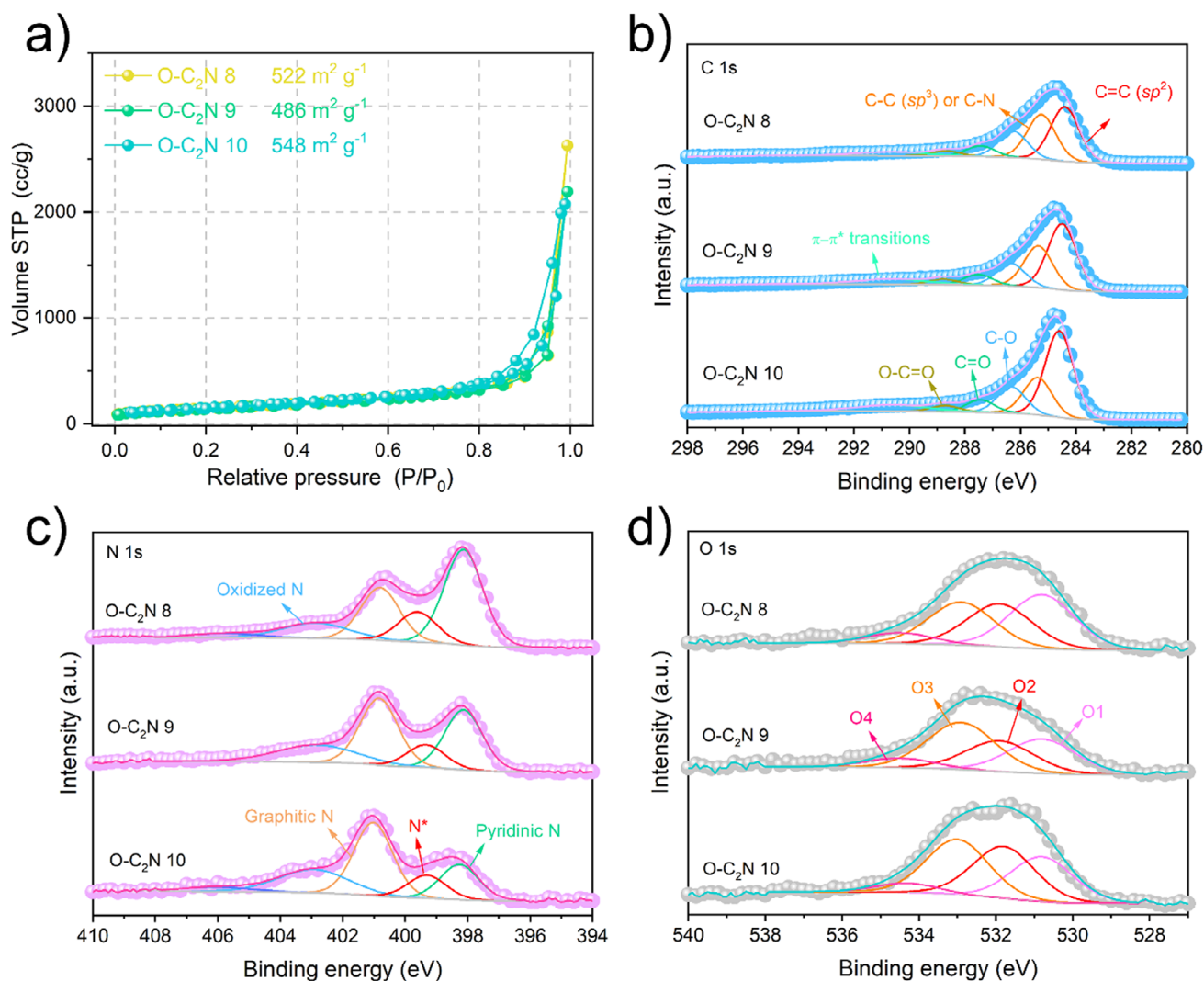


**Figure 2.** a) BET surface area of O-C<sub>2</sub>N catalysts. High-resolution XPS b) C 1s, c) N 1s and d) O 1s spectra of O-C<sub>2</sub>N 8, O-C<sub>2</sub>N 9 and O-C<sub>2</sub>N 10.

comparison purpose, the corresponding XPS analyses of O-C<sub>2</sub>N 8 and O-C<sub>2</sub>N 9 were also conducted. As shown in Figure 2b, XPS C 1s spectra of O-C<sub>2</sub>N samples exhibited five main characteristic peaks corresponding to sp<sup>2</sup> C=C (284.6 eV), sp<sup>3</sup> C-C or C-N bond (285.4 eV), C-O species (286.3 eV), C=O (287.4 eV) and O-C=O functionalities (288.7 eV). Compared to O-C<sub>2</sub>N 8 and O-C<sub>2</sub>N 9, it was indicated that the O-C<sub>2</sub>N 10 obtained from a higher condensation temperature exhibits a higher ratio/intensity of sp<sup>2</sup> carbon, while that of C-N (or sp<sup>3</sup> C-C) decreases slightly (Table S2). This is mainly attributed to the gradual removal of N species and elimination of those C defects under elevated temperatures, which might in turn reform the O microenvironment on the final carbon catalysts. The higher ratio of π-π\* transitions in O-C<sub>2</sub>N 10 (Table S2) also indicates a strong conjugated incorporation of those as-formed O functionalities in the carbon skeleton that certainly changes the support electrons for CO<sub>2</sub> catalysis. Further insights into the dynamic transformation of N/O species were also obtained by performing the XPS N1s and O1s spectra.

From Figure 2c, it is obvious that the intensity of pyridinic N decreases significantly at higher temperatures (e.g., O-C<sub>2</sub>N 9 and O-C<sub>2</sub>N 10), together with an increased ratio of graphitic N, suggesting a thermal rearrangement of N species. Throughout this process, the overall N content in the O-C<sub>2</sub>N also decreases significantly from 18 at% to 7 at% upon an increased annealing temperature, indicative of the removal of thermally unstable N species, as described previously.<sup>[20]</sup> Notably, the removal of N heteroatoms generally tends to create structural defects in a carbon skeleton. However, the rearrangement of carbon rings at elevated temperature will lead to the elimination of those vacancy sites and a thermal sintering of nanopores in the final catalysts, improving the graphitic structure, as evidenced by the Raman analysis (Figure S5). Such a dynamic transformation of surface chemical environment was further validated by XPS O 1s spectra (Figure 2d), showing a conversion of carbonyl groups and C-O species. Specifically, at higher temperatures, the ratio of O 1s characteristic peak at 531 ± 0.2 eV (O1) decreases significantly, corresponding to the carbonyl C=O that might

be eliminated during pyrolysis due to a relatively low thermal stability.<sup>[27,33]</sup> In contrast, two peaks at  $531.8 \pm 0.2$  (O2) and  $533 \pm 0.2$  eV (O3) increase evidently in the O 1s spectra of O-C<sub>2</sub>N 9 and 10, indicating the apparent emergence of ring epoxy (or hydroxyl, O2) and aromatic in-plane ether groups (O3) at high temperatures.<sup>[22,34–36]</sup> Thus, despite the gradual removal of N species (mainly pyridinic), an increased graphitic structure (dominated by sp<sup>2</sup> C=C) is obtained in O-C<sub>2</sub>N catalysts after high-temperature pyrolysis that may lead to an altered catalytic behaviour.

To give more in-depth understanding of the local oxygen bonding chemistry in the as-prepared O-C<sub>2</sub>N catalysts, near-edge X-ray absorption fine structure (NEXAFS) measurements were further conducted. As can be seen from Figure 3a, the NEXAFS C K-edge spectra of O-C<sub>2</sub>N 10 exhibits two characteristic peaks at 287.6 and 288.3 eV, which corresponds to the C 1s →  $\pi^*$  transitions of C–O–C and C=O moieties, respectively, echoing with the XPS results for epoxy and carbonyl O. Notably, in the C K-edge NEXAFS spectra of O-C<sub>2</sub>N 8 and 9, no obvious  $\pi^*(\text{C–O–C})$  resonance can be detected, suggesting the lack of apparent single-bonded C–O–C feature in the samples obtained from lower condensation temperatures. This can be further supported by the O K-edge NEXAFS measurements (Figure 3c). At lower photon energy side, the nearly absent appearance of  $\pi^*(\text{C=O})$  transition characteristic in the O K-edge NEXAFS spectra of O-C<sub>2</sub>N 10 evidently indicates the possible elimination of carbonyl O at high temperatures, in consistency with the XPS analysis for a reformed O microenvironment. This is mainly ascribed to the thermally less stable nature of O functional groups containing  $\pi^*$  carbonyl orbitals than those of formally single-bonded C–O–C species, as reported previously.<sup>[37]</sup> The evident emergence of  $\pi^*$  transition peak of C–O–C bond at around 535.4 eV in the O K-edge NEXAFS spectra of O-C<sub>2</sub>N 10 further supports such observation that the high-temperature chemistry employed has led to the rearrangement of surface O microenvironment where C–O–C functionalities (e.g., ring epoxy or in-plane ether) become the dominant species.<sup>[38]</sup> By contrast, the much lower intensity of this  $\pi^*$  transition resonance in O-C<sub>2</sub>N 8 and 9 suggests the different coverages of surface C–O–C groups that are not the dominant O/C configuration in the lower temperature species, giving distinctive chemical feature for catalytic study.<sup>[39]</sup>

Similar to that observed in XPS N 1s spectra, the removal/conversion of pyridinic and pyrrolic N in O-C<sub>2</sub>N 10 was further validated by N K-edge NEXAFS spectra (Figure 3b), giving a significant decrease of signal intensity at 398.5 and 399.8 eV. By contrast, compared to that of O-C<sub>2</sub>N 8 and 9, the  $\pi^*$  transition resonance in the N K-edge NEXAFS spectrum of O-C<sub>2</sub>N 10 increases drastically at 401.5 eV, together with a positive shift by about 0.2 eV. This suggests an exocyclic O-substitution in the carbon skeleton near the N species, where possible N–C–O–C motifs are formed in O-C<sub>2</sub>N 10, consisting with an increased ratio of N\* (refers to pyridonic N–C–O species) in the XPS N1s spectra, as reported previously.<sup>[40]</sup> Collectively, the above X-ray spectroscopic results all indicate a thermal reformation of O microenvironment on O-C<sub>2</sub>N under high temperatures,

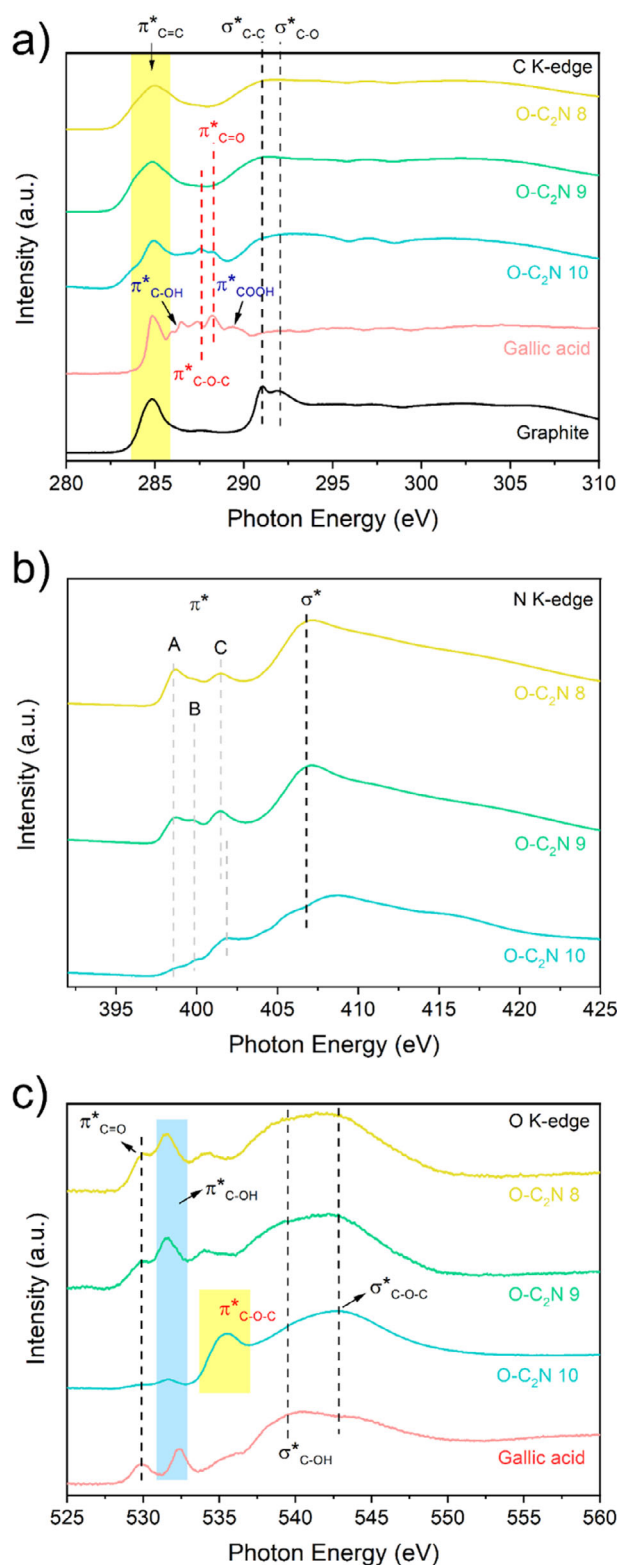


**Figure 3.** a) C, b) N and c) O K-edge near edge X-ray absorption fine structure (NEXAFS) spectra of the O-C<sub>2</sub>N catalysts and a gallic acid sample for comparison.

where single-bonded C—O—C functionalities (e.g., ring epoxy, in-plane ether) become the dominant oxygen substructures within O—C<sub>2</sub>N 10 catalysts that may afford abundant active N—C—O—C moieties for CO<sub>2</sub> electroreduction.

The electrochemical CO<sub>2</sub> reduction performance was first evaluated in a standard three-electrode H-cell system with CO<sub>2</sub>-saturated 0.1 M KHCO<sub>3</sub> solution (details can be found in the Supporting Information), where the anode and cathode chambers were separated by a Nafion membrane to avoid possible back-oxidation of CO<sub>2</sub>RR products. All potential values recorded during the electrochemical measurements were converted to the reversible hydrogen electrode (RHE) reference potential for facile comparison purpose. As shown in Figure 4a, the linear sweep voltammetry (LSV) curve of O—C<sub>2</sub>N 10 exhibited a much higher current density in CO<sub>2</sub>-saturated KHCO<sub>3</sub> solution than that in Ar-saturated electrolyte, suggesting a preferential CO<sub>2</sub>RR process on the O—C<sub>2</sub>N 10 catalysts. Further performing the CO<sub>2</sub>RR measurements reveals a lower catalytic activity on O—C<sub>2</sub>N 8 and O—C<sub>2</sub>N 9 compared to that of O—C<sub>2</sub>N 10 in terms of both onset and current density (Figure S6), indicative of the benefiting role of single-bonded O functionalities during CO<sub>2</sub>RR. To gain more insights into the CO<sub>2</sub>RR performance, the activity and selectivity of O—C<sub>2</sub>N 10 were further analysed by performing the bulk electrolysis under different potentials ranging from −0.6 to −1.2 V<sub>RHE</sub>, where the CO<sub>2</sub>RR products were quantified by gas chromatography (GC) and <sup>1</sup>H nuclear magnetic resonance (NMR). Notably, carbon monoxide (CO) and hydrogen (H<sub>2</sub>) were identified as the only gas products during the potentiostatic electrolysis, whereas no liquid products could be detected through NMR measurements. Interestingly, the O—C<sub>2</sub>N 10 electrocatalysts exhibited the highest activity and selectivity towards CO<sub>2</sub>RR among all comparison samples, demonstrating the advocating role of single-bonded C—O—C moieties in catalysing CO<sub>2</sub>RR within the carbon catalysts. Under an operation potential region from −0.6 to −0.8 V<sub>RHE</sub>, a high CO<sub>2</sub>-to-CO Faradaic efficiency (FE<sub>CO</sub>) of above 90% was retained (Figure 4b), reaching a FE<sub>CO</sub> of ~94.8% at −0.6 V<sub>RHE</sub>. Along with an increased overpotential, the FE<sub>CO</sub> decreases gradually due to the competing H<sub>2</sub> evolution reaction (HER) in the high potential range, which is however wanted, as it leads to a tunable syngas (CO/H<sub>2</sub>) ratio in the final product. This might be due to the appearance of doped N heteroatoms within the catalysts (especially those dominated graphitic N sites in O—C<sub>2</sub>N 10) where HER process tends to operate at high overpotentials.<sup>[15,20,41]</sup> To further investigate the CO<sub>2</sub>RR kinetics, Tafel slope analysis was also conducted (Figure S7), revealing a Tafel slope of 184.8 mV dec<sup>−1</sup> on O—C<sub>2</sub>N 10, which indicates the possible mass transfer (e.g., CO<sub>2</sub> adsorption and CO desorption) limitations during the CO<sub>2</sub> electroreduction.<sup>[42,43]</sup> For comparison, O—C<sub>2</sub>N catalysts fabricated under different temperature conditions were also tested for CO<sub>2</sub>RR. It is revealed that all electrocatalysts followed a similar selectivity trend with the changes of applied potential (Figure 4b), giving a high FE<sub>CO</sub> under relatively low overpotentials. Obtained from a higher thermal condensation temperature than O—C<sub>2</sub>N 8, the O—C<sub>2</sub>N 9 showed a higher catalytic CO<sub>2</sub>RR current density than that

of O—C<sub>2</sub>N 8 at all evaluated potentials, which might be attributed to the increased amount of single-bonded O species and a higher ratio of graphitic C that benefits a better activity and conductivity in O—C<sub>2</sub>N 9 (Figure 2d). However, despite a higher CO selectivity at −0.6 V<sub>RHE</sub>, the FE<sub>CO</sub> of O—C<sub>2</sub>N 9 decreases drastically and is close to that of O—C<sub>2</sub>N 8 at −0.8 and −1.0 V<sub>RHE</sub>. In contrast, O—C<sub>2</sub>N 10 revealed a much higher FE<sub>CO</sub> and partial current density at any given potentials than that of O—C<sub>2</sub>N 8 and O—C<sub>2</sub>N 9 (Figure 4c), and this carbocatalyst exhibits partial current density of 2.75 and 5.05 mA cm<sup>−2</sup> with selectivity of 94.8% and 89.3% for electrochemical CO<sub>2</sub> to CO conversion at −0.6 and −0.8 V<sub>RHE</sub>, respectively, suggesting the distinctively different active sites within O—C<sub>2</sub>N 10 compared to the other counterparts.

To this end, correlations between O substructures and CO<sub>2</sub>RR activity were analysed to investigate the genuine CO<sub>2</sub>-to-CO active species on O—C<sub>2</sub>N electrocatalysts. As shown in Figure S8, the ring epoxy and in-plane ether groups become the dominate oxygen functionalities in samples (O—C<sub>2</sub>N 9 and O—C<sub>2</sub>N 10) obtained from those elevated condensation temperatures, where higher CO<sub>2</sub>-to-CO partial current densities could be achieved. Further elevating the temperature to 1000 °C significantly altered the O microenvironment on O—C<sub>2</sub>N, giving dominant C—O—C features that differ largely from O—C<sub>2</sub>N 8 and O—C<sub>2</sub>N 9, especially based on O K-edge NEXAFS spectra (Figure 3c). As a result, the CO<sub>2</sub>-to-CO partial current density increases dramatically on O—C<sub>2</sub>N 10 and is 3.5 and 19.1 times higher than that on O—C<sub>2</sub>N 9 and O—C<sub>2</sub>N 8 at −0.8 V<sub>RHE</sub>, respectively (Figure 4c). Notably, both previous theoretical simulations and experiments suggested a strong electrostatic interaction between the polarizable CO<sub>2</sub> molecules and the lone pair electron-donating ether or epoxy groups via Lewis acid-base interactions.<sup>[44–46]</sup> Meanwhile, it is worth noting that no evident correlations between N species and CO productivity can be observed, echoing with the previous reports that N heteroatoms are not responsible for the genuine CO<sub>2</sub> electroreduction on defective mesoporous carbon.<sup>[20]</sup> Under high condensation temperature, it was typically suggested that the removal of N heteroatoms may generate sp<sup>3</sup>—C defects as possible active sites. In our case, compared with O—C<sub>2</sub>N 8 and O—C<sub>2</sub>N 9, an apparent decrease of sp<sup>3</sup>—C was identified in O—C<sub>2</sub>N 10 catalysts (Figure 2b), explained by the thermal sintering of defects and pores within the carbon skeleton, giving a negative correlation between those structural defects and catalytic performance. In contrast, the high thermal stability of single-bonded O functionalities endows O—C<sub>2</sub>N materials a good feasibility in fine tuning their local O microenvironment through simple pyrolysis method. Therefore, from the combined electrochemical measurements and spectroscopic characterizations, it was evidenced that the superior CO<sub>2</sub>-to-CO activity on the O—C<sub>2</sub>N 10 electrocatalysts is mainly attributed to those highly active and selective N—C—O—C species.

To evaluate the catalytic stability of the highly active and selective O—C<sub>2</sub>N 10 catalysts, chronoamperometry measurements were further employed under an applied voltage of −0.8 V<sub>RHE</sub>. Notably, no obvious changes of the cat-

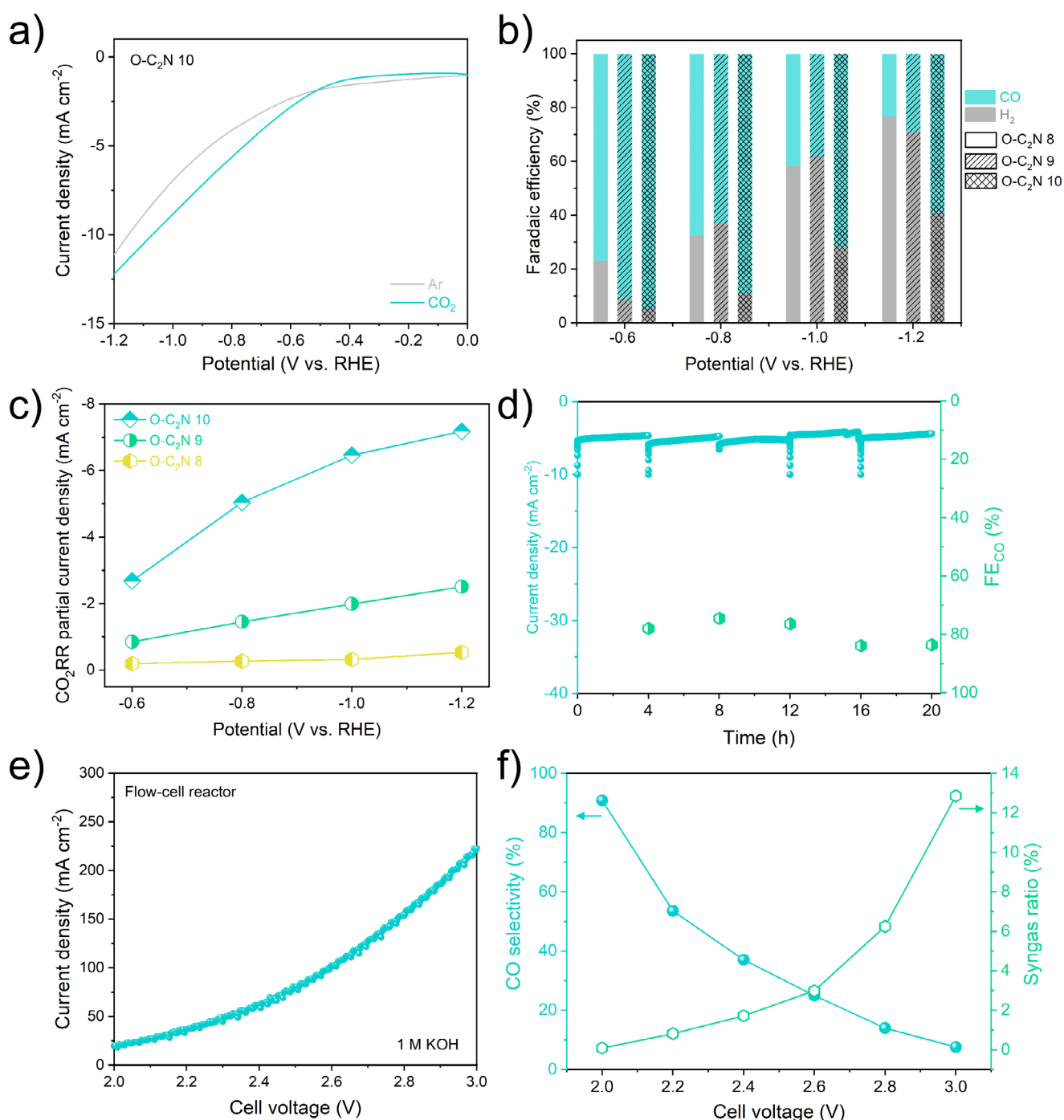


**Figure 4.** a) Linear sweep voltammetry of O-C<sub>2</sub>N 10 catalysts in Ar- and CO<sub>2</sub>-saturated 0.1 M KHCO<sub>3</sub> solution. b) Faradaic efficiencies of CO (cyan) and H<sub>2</sub> (grey) on O-C<sub>2</sub>N 8, 9 and 10 under different potentials. c) The partial current density of CO on O-C<sub>2</sub>N 8, 9 and 10 under a range of applied potentials. d) The CO<sub>2</sub>RR stability test of O-C<sub>2</sub>N 10 under the potential of -0.8 V<sub>RHE</sub> for over 20 h. e) The CO<sub>2</sub>RR performance of O-C<sub>2</sub>N 10 in a flow-cell reactor. f) The CO selectivity and the corresponding syngas ratio (H<sub>2</sub>:CO) on O-C<sub>2</sub>N 10 in a flow-cell reactor under different cell voltages.

alytic CO<sub>2</sub>RR performance can be observed for O-C<sub>2</sub>N 10 (Figure 4d), giving a well-retained current density as well as CO selectivity at around 5 mA cm<sup>-2</sup> and 80%, respectively, for over 20-h operation. Further conducting the post-reaction characterizations reveals negligible changes on O-C<sub>2</sub>N 10 after durability test (Figure S9), evidencing a structurally and chemically stable property of the catalysts. Compared with

that in bulk electrolysis, the slight decrease of CO selectivity during the stability test of O-C<sub>2</sub>N 10 is mainly attributed to the accumulation of products on catalysts within the applied static H-cell setup, where the mass/charge transfer process is severely limited.<sup>[47]</sup> In this regard, to quantify the catalytic CO<sub>2</sub>RR behaviour of the O-C<sub>2</sub>N 10 catalysts under more applied engineering conditions, a flow-cell reactor equipped



with a gas-diffusion electrode (GDE) setup was employed (Figure S10). As shown in Figure 4e, a current density of  $20.2 \text{ mA cm}^{-2}$  can be achieved at an overall cell voltage of 2 V, where a  $\text{CO}_2$ -to- $\text{CO}$  selectivity as high as 90.8% could be obtained (Figure 4f). Further increasing the operation cell voltages leads to an adjustable syngas ratio ( $\text{H}_2$ : $\text{CO}$ ) within the gas products of such flow reactor, which ranges from 0.1 to 6.25 in the wider potential window from 2 to 2.8 V (Figure 4f). This satisfies the application of  $\text{H}_2$ / $\text{CO}$  syngas in most chemical synthesis applications, including but not limited to the production of ethanol (e.g., <1) and methanol (e.g., ~2), Fischer-Tropsch process (e.g., >2) and synthetic fuels (e.g., 0.6).<sup>[48,49]</sup> Within our presented flow reactor, the composition of  $\text{CO}_2$ RR gas products on  $\text{C}_2\text{N}$  10 catalysts can be fine adjusted by simply changing the operation cell voltages in a practical flow reactor device, facilitating the integration of efficient  $\text{CO}_2$ RR process within a wide range of chemical industrial applications.

## Conclusion

In summary, through a programmable thermal condensation method, oxygen-substituted  $\text{C}_2\text{N}$  ( $\text{O}-\text{C}_2\text{N}$ ) frameworks with distinctive  $\text{C}-\text{O}-\text{C}$  functionalities were synthesized and employed as efficient electrocatalyst for  $\text{CO}_2$  electroreduction. Combined X-ray absorption spectroscopy and XPS characterizations all indicate the appearance of abundant and highly dispersed single-bonded  $\text{C}-\text{O}-\text{C}$  moieties (e.g., ring epoxy or in-plane ether) in  $\text{O}-\text{C}_2\text{N}$  10, while samples obtained from lower condensation temperatures tend to exhibit less  $\text{C}-\text{O}-\text{C}$  features with more  $\text{C}=\text{O}$  configurations, showing distinguishable functionality differences that can be correlated to different catalytic behaviours. Further conducting electrochemical measurements reveals a positive relationship between the presence of single-bonded  $\text{C}-\text{O}-\text{C}$  configurations and a high  $\text{CO}_2$ -to- $\text{CO}$  conversion, giving insights into the origin of  $\text{CO}$  selectivity in those oxygen and nitrogen incorporated carbon catalysts. Benefited from the porous feature and well-defined  $\text{C}-\text{O}-\text{C}$  active moieties within a N-doped carbon skeleton, the as-prepared  $\text{O}-\text{C}_2\text{N}$  10 catalysts can exhibit a high  $\text{CO}$  selectivity up to 94.8%, showing robust catalytic stability for at least over 20-h  $\text{CO}_2$ RR duration. Further employing  $\text{O}-\text{C}_2\text{N}$  10 in a flow-cell reactor delivers a tunable syngas ratio (ranges from 0.1 to 6.25) at high current densities, which offers great opportunities for integrated  $\text{CO}_2$  valorization. This work not only provides feasible strategy to fabricate the O-substituted carbon catalysts with well-controlled  $\text{C}-\text{O}-\text{C}$  configurations but also gives insights into the origin of the  $\text{CO}$  selectivity during  $\text{CO}_2$ RR by comparing the different O/N incorporated defective carbons.

## Acknowledgements

The work was supported by the National Natural Science Foundation of China (No. 52470053, U21A20160, 52373205 and 52003251), the Australian Renewable Energy Agency (ARENA 2018/RND014), Australian Research Council

(ARC) Training Centre for Global Hydrogen Economy (IC200100023), and ARC Centre of Excellence for Carbon Science and Innovation (CE230100032). Q.Z. would like to acknowledge the National Natural Science Foundation of China for Excellent Young Scientists Fund Program (Overseas, No. 04002350153) and the Fundamental Research Funds for the Central Universities (No. 04002150133, 0400219013/011) for the financial support of the work. R.D. acknowledges the financial support from UNSW Scientia Fellowship and ARC under Discovery Early Career Researcher Award (DE230101396). The work was supported by Max Planck Society that is gratefully acknowledged for financial and organizational support over many years.

## Conflict of Interests

The authors declare no conflict of interest.

## Data Availability Statement

The data that support the findings of this study are available from the corresponding author upon reasonable request.

**Keywords:**  $\text{C}_2\text{N}$  frameworks •  $\text{CO}_2$  reduction • Metal-free catalysts • Oxygen substitution • Syngas

- [1] T. Zheng, M. Zhang, L. Wu, S. Guo, X. Liu, J. Zhao, W. Xue, J. Li, C. Liu, X. Li, Q. Jiang, J. Bao, J. Zeng, T. Yu, C. Xia, *Nat. Catal.* **2022**, 5, 388–396.
- [2] Y. Xu, X. Li, J. Gao, J. Wang, G. Ma, X. Wen, Y. Yang, Y. Li, M. Ding, *Science* **2021**, 371, 610–613.
- [3] R. Daiyan, I. Macgill, R. Amal, *ACS Energy Lett.* **2020**, 5, 3843–3847.
- [4] S. Verma, S. Lu, P. J. A. Kenis, *Nat. Energy* **2019**, 4, 466–474.
- [5] Y. Y. Birdja, E. Pérez-Gallent, M. C. Figueiredo, A. J. Göttle, F. Calle-Vallejo, M. T. M. Koper, *Nat. Energy* **2019**, 4, 732–745.
- [6] X. Duan, J. Xu, Z. Wei, J. Ma, S. Guo, S. Wang, H. Liu, S. Dou, *Adv. Mater.* **2017**, 29, 1701784.
- [7] J. Gu, C. S. Hsu, L. Bai, H. M. Chen, X. Hu, *Science* **2019**, 364, 1091–1094.
- [8] L. Wang, D. C. Higgins, Y. Ji, C. G. Morales-Guio, K. Chan, C. Hahn, T. F. Jaramillo, *Proc. Natl. Acad. Sci. USA* **2020**, 117, 12572–12575.
- [9] L. Li, Z. Zhao, C. Hu, P. Yang, X. Yuan, Y. Wang, L. Zhang, L. Moskalova, J. Gong, *ACS Energy Lett.* **2020**, 5, 552–558.
- [10] B. Kim, H. Seong, J. T. Song, K. Kwak, H. Song, Y. C. Tan, G. Park, D. Lee, J. Oh, *ACS Energy Lett.* **2020**, 5, 749–757.
- [11] T. T. Zhuang, Z. Q. Liang, A. Seifitokaldani, Y. Li, P. De Luna, T. Burdyny, F. Che, F. Meng, Y. Min, R. Quintero-Bermudez, C. T. Dinh, Y. Pang, M. Zhong, B. Zhang, J. Li, P. N. Chen, X. L. Zheng, H. Liang, W. N. Ge, B. J. Ye, D. Sinton, S. H. Yu, E. H. Sargent, *Nat. Catal.* **2018**, 1, 421–428.
- [12] M. Antonietti, M. Oschatz, *Adv. Mater.* **2018**, 30, 1706836.
- [13] Z. Tian, Q. Zhang, T. Liu, Y. Chen, M. Antonietti, *ACS Nano* **2024**, 18, 6111–6129.
- [14] R. Daiyan, X. Zhu, Z. Tong, L. Gong, A. Razmjou, R.-S. Liu, Z. Xia, X. Lu, L. Dai, R. Amal, *Nano Energy* **2020**, 78, 105213.



- [15] Y. Dong, Q. Zhang, Z. Tian, B. Li, W. Yan, S. Wang, K. Jiang, J. Su, C. W. Oloman, E. L. Gyenge, R. Ge, Z. Lu, X. Ji, L. Chen, *Adv. Mater.* **2020**, 32, 1–10.
- [16] Q. Zhang, Y. Chen, J. Pan, R. Daiyan, E. C. Lovell, J. Yun, R. Amal, X. Lu, *Small* **2023**, 19, 2302338.
- [17] H. Wang, J. Jia, P. Song, Q. Wang, D. Li, S. Min, C. Qian, L. Wang, Y. F. Li, C. Ma, T. Wu, J. Yuan, M. Antonietti, G. A. Ozin, *Angew. Chem. Int. Ed.* **2017**, 129, 7955–7960.
- [18] J. Wu, M. Liu, P. P. Sharma, R. M. Yadav, L. Ma, Y. Yang, X. Zou, X.-D. Zhou, R. Vajtai, B. I. Yakobson, J. Lou, P. M. Ajayan, *Nano Lett.* **2016**, 16, 466–470.
- [19] J. Wu, R. M. Yadav, M. Liu, P. P. Sharma, C. S. Tiwary, L. Ma, X. Zou, X. Zhou, B. I. Yakobson, J. Lou, P. M. Ajayan, *ACS Nano* **2015**, 9, 5364–5371.
- [20] R. Daiyan, X. Tan, R. Chen, W. H. Saputera, H. A. Tahini, E. Lovell, Y. H. Ng, S. C. Smith, L. Dai, X. Lu, R. Amal, *ACS Energy Lett.* **2018**, 3, 2292–2298.
- [21] D. S. S. Jian Zhang, X. i Liu, R. Blume, A. Zhang, R. Schlögl, *Science* **2008**, 322, 73–77.
- [22] Q. Zhang, X. Tan, N. M. Bedford, Z. Han, L. Thomsen, S. Smith, R. Amal, X. Lu, *Nat. Commun.* **2020**, 11, 4181.
- [23] X. Lu, W. L. Yim, B. H. R. Suryanto, C. Zhao, *J. Am. Chem. Soc.* **2015**, 137, 2901–2907.
- [24] F. Yang, X. Ma, W. Cai, P. Song, W. Xu, *J. Am. Chem. Soc.* **2019**, 141, 20451–20459.
- [25] S. Yamamoto, K. Takeuchi, Y. Hamamoto, R. Y. Liu, Y. Shiozawa, T. Koitaya, T. Someya, K. Tashima, H. Fukidome, K. Mukai, S. Yoshimoto, M. Suemitsu, Y. Morikawa, J. Yoshinobu, I. Matsuda, *Phys. Chem. Chem. Phys.* **2018**, 20, 19532–19538.
- [26] D. Wu, J. Liu, Y. Yang, Y. Zheng, *Ind. Eng. Chem. Res.* **2020**, 59, 14055–14063.
- [27] E. Jung, H. Shin, B. H. Lee, V. Efremov, S. Lee, H. S. Lee, J. Kim, W. Hooch Antink, S. Park, K. S. Lee, S. P. Cho, J. S. Yoo, Y. E. Sung, T. Hyeon, *Nat. Mater.* **2020**, 19, 436–442.
- [28] Z. Tian, N. López-Salas, C. Liu, T. Liu, M. Antonietti, *Adv. Sci.* **2020**, 7, 1–17.
- [29] Z. Tian, N. Fechner, M. Oschatz, T. Heil, J. Schmidt, S. Yuan, M. Antonietti, *J. Mater. Chem. A* **2018**, 6, 19013–19019.
- [30] Z. Tian, Q. Zhang, L. Thomsen, N. Gao, J. Pan, R. Daiyan, J. Yun, J. Brandt, N. López-Salas, F. Lai, Q. Li, T. Liu, R. Amal, X. Lu, M. Antonietti, *Angew. Chem. Int. Ed.* **2022**, 61, e202206915.
- [31] X. Liu, C. Giordano, M. Antonietti, *Small* **2014**, 10, 193–200.
- [32] H. Yang, Y. Wu, Q. Lin, L. Fan, X. Chai, Q. Zhang, J. Liu, C. He, Z. Lin, *Angew. Chem. Int. Ed.* **2018**, 57, 15476–15480.
- [33] J. J. M. O. J. L. Figueiredo\*, M. F. R. Pereira, M. M. A. Freitas, *Carbon* **1999**, 37, 1379–1389.
- [34] R. Larciprete, S. Gardonio, L. Petaccia, S. Lizzit, *Carbon* **2009**, 47, 2579–2589.
- [35] C. Vol, E. Science, G. Britain, C. Technik, U. Karlsruhe, A. Germany, *Carbon* **1996**, 34, 983–998.
- [36] Y. Lin, K. H. Wu, Q. Lu, Q. Gu, L. Zhang, B. Zhang, D. Su, M. Plodinec, R. Schlögl, S. Heumann, *J. Am. Chem. Soc.* **2018**, 140, 14717–14724.
- [37] A. Kuznetsova, I. Popova, J. T. Yates, M. J. Bronikowski, C. B. Huffman, J. Liu, R. E. Smalley, H. H. Hwu, J. G. Chen, *J. Am. Chem. Soc.* **2001**, 123, 10699–10704.
- [38] J. B. Kortright, J. Sun, R. K. Spencer, X. Jiang, R. N. Zuckermann, *J. Phys. Chem. B* **2017**, 121, 298–305.
- [39] D. D'Angelo, C. Bongiorno, M. Amato, I. Deretzis, A. La Magna, E. Fazio, S. Scalese, *J. Phys. Chem. C* **2017**, 121, 5408–5414.
- [40] P. Leinweber, J. Kruse, F. L. Walley, A. Gillespie, K. U. Eckhardt, R. I. R. Blyth, T. Regier, *J. Synchrotron Radiat.* **2007**, 14, 500–511.
- [41] Z. Lin, Y. Yang, M. Li, H. Huang, W. Hu, L. Cheng, W. Yan, Z. Yu, K. Mao, G. Xia, J. Lu, P. Jiang, K. Yang, R. Zhang, P. Xu, C. Wang, L. Hu, Q. Chen, *Angew. Chem. Int. Ed.* **2019**, 58, 16973–16980.
- [42] M. Li, H. Wang, W. Luo, P. C. Sherrell, J. Chen, J. Yang, *Adv. Mater.* **2020**, 32, 2001848.
- [43] E. Lepre, J. Heske, M. Nowakowski, E. Scoppola, I. Zizak, T. Heil, T. D. Kühne, M. Antonietti, N. López-Salas, J. Alberio, *Nano Energy* **2022**, 97, 107191.
- [44] B. Petrovic, M. Gorbounov, S. M. Soltani, *Carbon Capture Sci. Technol.* **2022**, 3, 100045.
- [45] B. Petrovic, M. Gorbounov, S. M. Soltani, *Microporous Mesoporous Mater.* **2021**, 312, 110751.
- [46] Y. Liu, J. Wilcox, *Environ. Sci. Technol.* **2013**, 47, 95–101.
- [47] Q. Chen, X. Wang, Y. Zhou, Y. Tan, H. Li, J. Fu, M. Liu, *Adv. Mater.* **2024**, 36, 1–26.
- [48] H. Khosravani, M. Meshksar, H. R. Rahimpour, M. R. Rahimpour, in *Advances in Synthesis Gas: Methods, Technologies and Applications*, Vol. 3, Elsevier, Amsterdam **2022**, pp. 3–25.
- [49] H. J. Chae, J. Kim, S. C. Lee, H. Kim, S. Bin Jo, J. Ryu, T. Y. Kim, C. H. Lee, S. J. Kim, S. Kang, J. C. Kim, M. Park, *Catalysts* **2020**, 10, 99.

Manuscript received: January 22, 2025

Revised manuscript received: March 13, 2025

Accepted manuscript online: March 23, 2025

Version of record online: April 10, 2025